Optimizing Rice Field Mapping in the Northern Region of China: An Asynchronous Flooding Signal and Object-Based Method

Long Li, Daoqin Zhou, Kai Liu, Tian Shi, Chou Xie, Shudong Wang, Hang Li, Guannan Dong, and Xueke Li

***Abstract*—Accurate delineation of paddy fields holds importance in ensuring food security, efficient water resource management, and precise evaluation of greenhouse gas emissions. Here we propose an innovative approach, the asynchronous flooding and object-based (AF-OB) model, aimed at optimizing phenology-based paddy field mapping. The AF-OB model capitalizes on the asynchronous flooding phenomenon observed between paddy fields and nonpaddy fields, along with the seasonal variations in the normalized difference vegetation index. The simple noniterative clustering algorithm is integrated to mitigate the common issue of the "pretzel effect" encountered in paddy field mapping. Evaluation through independent samples yields compelling results, with the paddy field map generated by the AF-OB method achieving an overall accuracy of 94.28%. The paddy fields extracted using the AF-OB method exhibit alignment with statistical data, surpassing comparable algorithms relying on alternative land use products in terms of visual quality. Furthermore, the AF-OB model exhibits stability across time, space, and sensors, thus enhancing its applicability and robustness. The outputs of the AF-OB method offer reference data for informed agricultural production planning and the effective management of water resources.**

Manuscript received 18 September 2023; revised 11 December 2023 and 11 January 2024; accepted 16 January 2024. Date of publication 23 January 2024; date of current version 1 February 2024. This work was supported in part by the National Natural Science Foundation of China under Grant 42141007 and Grant 41671362, in part by the Key Program of Aerospace Information Innovation Institute of Chinese Academy of Sciences under Grant E2Z211020F, in part by the Key Special Project for the Action of "Revitalizing Mongolia through Science and Technology" under Grant 2022EEDSKJXM003, and in part by the Science and Technology Plan Project of Hohhot under Grant 2022-Social-Key-4-1-1. *(Corresponding authors: Kai Liu; Tian Shi.)*

Long Li, Kai Liu, Shudong Wang, and Hang Li are with the State Key Laboratory of Remote Sensing Science, Aerospace Information Research Institute, Chinese Academy of Sciences, Beijing 100094, China (e-mail: lilong221@mails.ucas.ac.cn; liuk@aircas.ac.cn; wangsd@aircas.ac.cn; lihang02@aircas.ac.cn).

Daoqin Zhou and Tian Shi are with the Third Surveying and Mapping Institute of Guizhou Province, Guiyang 550000, China (e-mail: 214955874@qq.com; 783683980@qq.com).

Chou Xie is with the Aerospace Information Research Institute, Chinese Academy of Sciences, Beijing 100094, China (e-mail: xiechou@aircas.ac.cn).

Guannan Dong is with the Key Laboratory of Water Cycle & Related Land Surface Processes, Institute of Geographic Sciences and Natural Resources, Chinese Academy of Sciences, Beijing 100101, China (e-mail: dongguannan0517@igsnrr.ac.cn).

Xueke Li is with the Department of Earth and Environmental Science, University of Pennsylvania, Philadelphia, PA 19104 USA (e-mail: xuekeli@sas.upenn.edu).

This article has supplementary downloadable material available at https://doi.org/10.1109/JSTARS.2024.3357141, provided by the authors.

Digital Object Identifier 10.1109/JSTARS.2024.3357141

***Index Terms*—Google earth engine, paddy field mapping, phenology, simple noniterative clustering (SNIC) and object-based.**

I. Introduction

PADDY rice is one of the world's most important food crops, feeding a quarter of the world's population while occupying only about 12% of the world's arable land [3], [4]. Due to its unique growing conditions and high food production, paddy fields play an important role in water security and food security issues [6]. Rice consumes a significant amount of water during its growth, with water consumption being 2–3 times higher than that of other grains such as wheat or corn [8]. The rapid population growth and intensifying competition for nonagricultural water resources will impose challenges on regional water management [10], [11], particularly concerning rice production [12], [13]. In the Northern Region of China, where water scarcity is already a critical issue, the pressure on water management will be further exacerbated by the demands of rice cultivation [14], [15]. Consequently, it is crucial to develop timely and effective mapping methods for paddy fields that can provide accurate spatial information. This spatial data are essential for effective agricultural [16] and water resources management [17], [18].

Remote sensing technology offers several advantages over traditional field survey methods, including wide coverage, simplicity, and speed [19], [20], [21]. It enables the rapid mapping of the spatial pattern of paddy fields in both current and historical regions [19], [22]. Machine learning methods have consistently demonstrated high accuracy in paddy field mapping, primarily attributed to their capacity to effectively leverage multisource and multiseasonal remote sensing data concurrently [23], [24], [25], [26]. Machine learning enables the incorporation of features from synthetic aperture radar (SAR) data, mitigating the impact of cloud cover, and facilitates the utilization of multiseasonal data in conjunction with phenological information, thereby enhancing classification accuracy [23], [27], [28]. Nevertheless, machine learning often falls short in adequately addressing classification mechanisms. The lack of transparency poses challenges in comprehending the individual features' contributions to the final classification result [29], [30], particularly when dealing with a large number of features [31].

Hence, phenological models that analyze the dynamics of "bare soil-water-vegetation" during the rice reproductive period have been utilized in paddy field mapping studies [32]. This

model type heavily depends on detecting flood signals during the rice transplanting period [18], [33]. While some new models have emerged for paddy field mapping in recent years, such as those based on the "V" shaped time-series characteristics of VH backscattering from SAR data [2], [34] and models that consider greater LSWI variability in rice fields compared to drylands [35]. Most of these models has not been verified in large-scale paddy mapping studies. In the realm of optical remote sensing data, the most widely recognized algorithms for mapping paddy fields are the subtraction algorithms, developed by comparing the difference between the normalized difference vegetation index (NDVI) or enhanced vegetation index (EVI) and the land surface water index (LSWI) [32], [36].

This algorithm defines pixels with LSWI $+ \alpha >$ NDVI (or EVI) during transplanting as paddy fields, where α is a threshold value determined based on the specific conditions of the study area [5], [37], [38]. The model's simplicity and ease of implementation have contributed to its widespread validation in large-scale paddy field mapping efforts [33]. However, the model is susceptible to wetlands and thin clouds, leading many studies to utilize cropland masks to exclude noncropland pixels and minimize commission errors [39]. These cropland masks commonly rely on pre-existing land-use products or period-specific vegetation index thresholds, as well as slope thresholds [4], [7], [9]. Nonetheless, the reliance on land-use products and the regional specificity of the thresholds limit the method's generalizability and applicability [9]. At the same time, almost all phenology-based rule algorithms are pixel-based, resulting in a pronounced "pretzel effect" in the results of paddy field mapping, especially when using high-resolution remotely sensed imagery [9], [33].

In light of these considerations, this study aims to optimize the determination of cropland masks and flooding pixels. The seasonal dynamics of NDVI and flooding frequency of paddy fields are leveraged on GEE to propose an effective model for paddy field mapping based on dense satellite images. This model takes into account factors such as data accessibility and capitalizes on the benefits of optical image data in regions with limited cloud cover. The integration of phenology-based techniques with the capabilities of GEE harnesses the power of cloud computing to process vast amounts of data, thus paving the way for a more efficient and accurate approach to paddy field remote sensing mapping. The efficacy of the proposed model is evaluated within the Northern Region of China, a large-scale region characterized by its expansive landscape diversity and varied climatic conditions. The geographical context of the Northern Region of China offers a setting for the validation and testing of our model, allowing for insights into its efficacy within a region characterized by its agricultural landscape and dynamic climatic shifts. The objectives of this research are as follows:

1) to optimize the determination of cropland masks and flooded pixels;
2) to introduce object-based ideas into unsupervised regular phenology algorithms to reduce the "pretzel effect" in the results of paddy field mapping;
3) to validate the precision and reliability of the developed method through multiple datasets, ensuring its robustness across diverse landscapes and scenarios;
4) to evaluate the method's performance across varying temporal intervals, spatial extents, and sensor types, thereby establishing its adaptability and applicability under different circumstances.

II. Materials and Methods

A. Study Area

The study area for this research is situated in the Northern Region of China, which is the primary region for one-season rice production in the country. As per the 2020 statistics, rice production in the Northern Region of China accounted for approximately 19.93% of the total production [see Fig. 1(a)]. The study area is expansive, covering approximately five million square kilometers, and necessitates a minimum of 312 views of Landsat data to achieve complete coverage [see Fig. 1(b)]. Notably, the study area exhibits variations in topography and climate from east to west [40], [41]. The topography is dominated by plateaus, plains, and basins, with a higher elevation in the western part and lower elevation in the eastern part. Similarly, there is a general increase in regional annual precipitation and mean annual temperature from west to east [42], with most areas experiencing annual precipitation levels below 450 mm [43], [44], [45]. We mapped paddy fields in arid and semi-arid regions, including northwest China, that are often overlooked in many studies. Our study aims to validate the effectiveness and reliability of extraction methods for large paddy fields, with the objective of addressing food and water security issues in arid and semi-arid regions of China.

B. Dataset

The dataset available in this study can be divided into four categories: optical remote sensing data, sample data, statistical data, and other paddy field map products.

1) Landsat-8 OLI/TIRS: Atmospherically corrected Landsat 8 OLI/TIRS Collection 2 surface reflectance data were used for this study. It is worth noting that Landsat 8 operates on a 16-day repeat cycle, resulting in the possibility of acquiring the data up to 22 or 23 times per year [46]. To ensure the inclusion of flooding signals in paddy fields and minimize missed detections due to long repeat periods, a total of 5 years of data were collected.

To optimize the utilization of Landsat-8 OLI/TIRS observations and minimize the influence of cloud cover, only data with cloud cover less than 70% were included in this study. Cloud-covered areas within each image were identified and eliminated using bit masks. It is worth mentioning that the majority of data in the GEE platform is scaled for efficient storage. Therefore, the reflectance values of the images were converted using the scale and offset provided by the platform.

2) Samples of Paddy and Nonpaddy Fields: In this study, paddy samples and nonpaddy samples were collected using the GEE platform. The platform enables the filtering of Landsat-8 observations within a specified time period and provides access to Google high definition (HD) imagery, which assists in distinguishing between paddy fields and drylands. Particularly during specific periods like transplanting and harvesting, the differentiation between paddy fields and drylands in remote

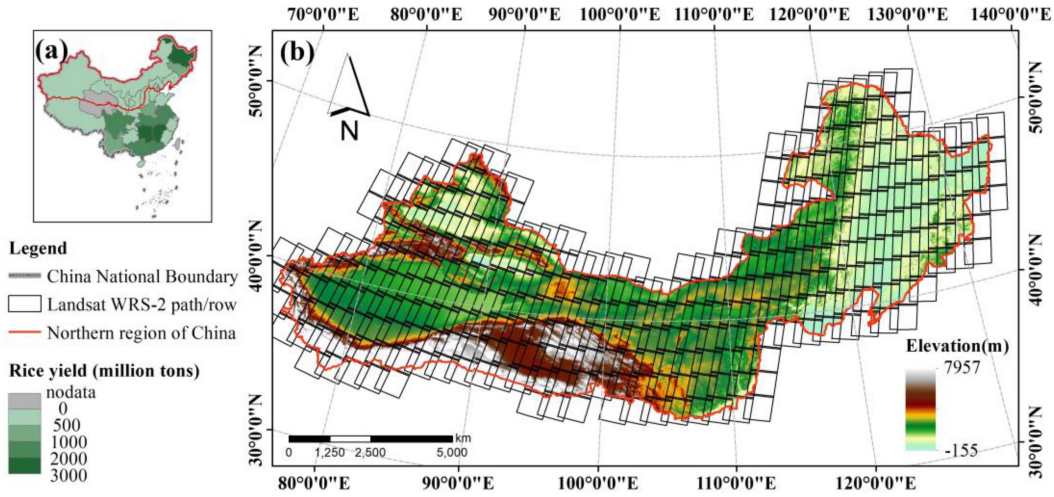

Fig. 1. (a) Location of the study area in China and rice production in Chinese provinces. (b) Study area topography and Landsat WRS-2 path/row.

sensing images tends to be clear. Landsat-8 images taken during these periods can indicate whether a pixel represents a paddy field or not [see Fig. 2(d)–(g)].

The determination and collection process of paddy field samples in this study was designed [see Fig. 2(a)]. Between approximately 110–130 days, paddy field pixels appear dark blue when displayed using the short-wave infrared, green, and blue bands for RGB visualization [see Fig. 2(d) and (e)]. This is because paddy fields exhibit similar characteristics to water bodies during the transplanting period, and the short-wave infrared band is highly sensitive to moisture signals [47]. At around 240–270 days, paddy pixels appear yellow-green when displayed in true color [see Fig. 2(f) and (g)]. This change in color is due to the maturation of rice, and the green-to-yellow transition is a commonly used characteristic in paddy mapping studies [48], [49], [50]. Band reflectance can also assist us in determining paddy field pixels, especially for flooding signals on days 110–130. Some of the Google HD images also exhibit these characteristics during the harvest period. In addition, in Google HD images, the paddy fields are typically divided into numerous small grids [see Fig. 2(b) and (c)]. This division is a result of rice cultivation being confined to flooded fields, and it is easier to manage and irrigate smaller fields [32].

A total of 1079 paddy field samples and 1007 nonpaddy field samples were collected using the above judgmental rules [see Fig. 2(j)]. The nonpaddy field samples included wetland, forest, and dryland areas. Out of these samples, 200 paddy field samples and 400 nonpaddy field samples were selected to generate frequency histograms for determining threshold values. The frequency histograms were used to establish thresholds that can effectively discriminate between paddy fields and nonpaddy fields. These thresholds were determined based on the characteristics observed in the histograms.

The remaining samples, which were not used for generating frequency histograms, were employed to validate the accuracy of the paddy field mapping. While the validation samples were not directly obtained from field surveys, we conducted on-site validation of a subset of paddy field samples. In addition, high-definition imagery from Google Earth was utilized to validate the accuracy of the samples. All samples underwent examination by two researchers, with any instances of inconsistent interpretations leading to the exclusion of the respective samples, thus ensuring the highest possible reliability. These validation samples allowed for an assessment of the mapping results and indicated the overall accuracy of the classification technique used in the study. By using separate subsets of samples for histogram analysis and accuracy validation, the study ensured an unbiased evaluation of the paddy field mapping approach and provided reliable results regarding the effectiveness of the discriminant rules and threshold values.

3) Agricultural Statistics: Statistical data from the China Statistical Yearbook and the Third National Land Resources Survey (NLRS) were collected to validate the mapping results of paddy fields. The China Statistical Yearbook is an annual publication that is compiled and published by local statistical bureaus in China. It acts as a repository of extensive statistics across multiple sectors, encompassing areas such as agriculture and industry. These statistics, accessible at http://www.stats.gov.cn/, find broad utilization within remote sensing applications for validating and monitoring crop cultivation areas [51], [52], [53].

The Third NLRS harnessed high-resolution satellite remote sensing imagery to generate foundational survey maps. Moreover, a three-year campaign of on-site investigations and meticulous manual analysis was undertaken, involving a workforce of 219 000 surveyors. This concerted endeavor culminated in the aggregation of data from a staggering 295 million survey patches, yielding an insight into China's land-use landscape [54]. To ensure the currency and precision of the survey outcomes, the Ministry of Natural Resources of China orchestrates annual assessments of land-use changes. These assessments serve to refresh the amassed data (https://gtdc.mnr.gov.cn/shareportal#/). However, it is important to note that these data do not include raster data with geographic coordinates, but rather includes area statistical tables and PDF-format maps.

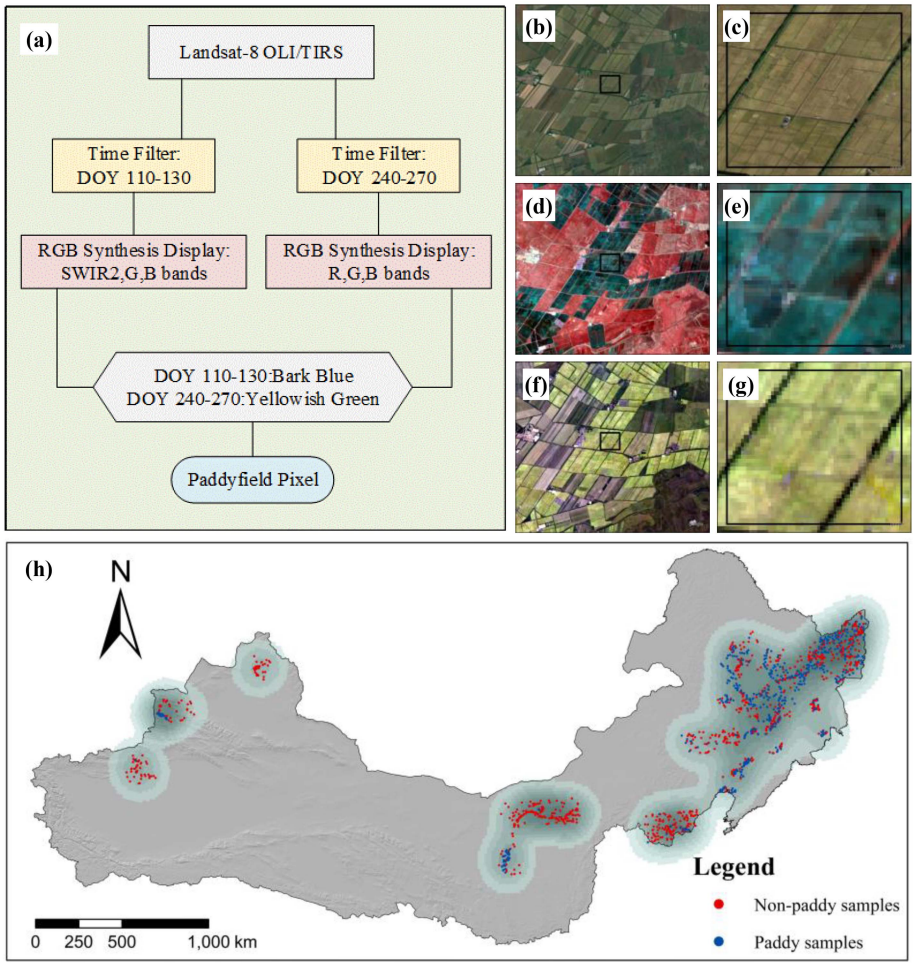

Fig. 2. Process and rules for determining paddy field samples. (a) Process for the determination of paddy field samples. (b), (c) Paddy fields in Google HD images. (d), (e) Landsat-8 image displayed as a composite of short-wave infrared, green, and blue bands during days 110–130. (f), (g) Landsat-8 images displayed in true color during 240–270 days. (h) Spatial distribution of samples.

4) Existing Rice Map: The NESEA-Rice10 database is a integration of data from MODIS, Sentinel-2, and Sentinel-1 satellites, along with various land cover products. This integration enables the construction of a detailed 10 m spatial resolution database of rice maps for Southeast Asia and Northeast Asia, covering the years 2017 to 2019. The NESEA-Rice10 database aligns with agricultural statistical data and provides detailed spatial information regarding the distribution of paddy fields [33]. For access to the NESEA-Rice10 data, you can download it from the following link: (https://zenodo.org/record/5645344).

C. Methods

This study employs a flooding pixel determination rule that takes into account the absolute reflectance of the band. Using this rule, paddy fields in the study area are mapped by utilizing asynchronous flooding frequency with simple noniterative clustering (SNIC). The unique flooding signal exhibited by paddy fields compared to dry land is attributed to the fact that rice is the only crop that requires transplantation in a mixed soil and water environment [55]. As a result, the detection of flooding signals has become widely adopted in paddy field mapping studies [2], [33], [34], [36], [37].

This study aims to detecting flooding signals to map paddy fields and proposes a new rule to define flooding pixels without other land cover products. The paddy field index, wetland index, and cropland index were calculated by the difference in seasonal dynamics of flooding frequency and NDVI between paddy fields and other land types in different periods. The three indices were superimposed and segmented using SNIC. Finally, thresholds were determined from a small number of samples to generate the paddy field mapping results. The results of paddy field mapping were validated by independent samples and compared with other paddy field mapping products.

1) Paddy Field Phenology Analysis: We analyzed time series curves of NDVI, LSWI, and each band through the paddy fields in the Northern Region of China. LSWI gradually decreases and is lower than NDVI around days 0–100, then increases rapidly and exceeds NDVI around 150. NDVI keeps increasing after day 160 and again exceeds LSWI, peaks between days 190 and 260, and then gradually decreases. On both day 50 and day 150, LSWI was higher than NDVI [see Fig. 3(a)], however on day

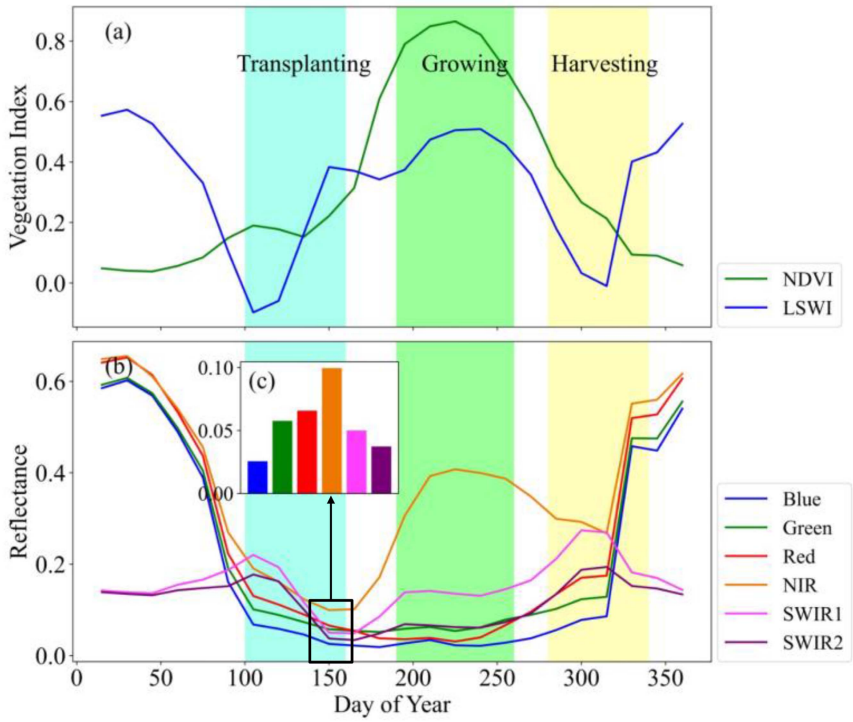

Fig. 3. Time series plots of paddy field vegetation indices and various bands. (a) NDVI and LSWI time series curve of the paddy field. (b) Time series curve of each band of the paddy field. (c) Band characteristics when the paddy field was flooded on day 150.

150 reflectance was very low in all bands and moisture-sensitive SWIR reached its lowest point of the year [see Fig. 3(b) and (c)].

It is shown that the bare soil of the cropland is gradually flooded with water and is in the transplanting period on days 100–150. NDVI reached its peak and was in the growing period on days 190—260. At days 270–340, NDVI gradually decreased to the lowest and was in the harvesting period [see Fig. 3(a) and (b)]. In determining these three periods, there is a transition of "bare soil-water body-vegetation-bare soil" in the state of the paddy field. The characteristics of these three periods allow to distinguish paddy fields from other land cover types.

2) Defining Flooded Pixels: The classical LSWI-NDVI>0 subtraction model was used for the definition of flooded pixels. However, due to the difficulty of removing cloud and snow edges using "QA_PIXEL" in GEE, averaging in the visible band was used to further minimize the effects of clouds and snow. The model only detects pixels with NDVI < 0.3 to avoid anomalies caused by high water content in the vegetation canopy. The flooded pixels are defined by the following equation:

$$\text{Flooded Pixel} = \begin{cases} 1 & \text{Mean (R, G, B)} < 0.1, \text{LSWI} - \text{NDVI} > 0, \text{NDVI} < 0.3 \\ 0 & \text{Other values} \end{cases} \tag{1}$$

where Mean (R, G, B) denotes the mean of the red band, the green band, and the blue band.

3) Cropland Index for Identification of Cropland Pixels: Due to the transplanting period of rice, the NDVI of paddy fields has the ability to vary greatly between the transplanting and growing periods. The cropland index in the study was designed by the seasonal dynamic characteristics of NDVI in paddy fields with reference to the seasonal dynamic index [56]. The study used a designed cropland index to separate cropland from noncropland

$$\text{Cropland index} = \frac{\text{NDVI (Growing)} - \text{NDVI (Transplanting)}}{\text{NDVI (Growing)} + \text{NDVI (Transplanting)}}. \tag{2}$$

4) Asynchronous Flooding Characteristics: The study used the Paddy index (flooding frequency of the transplanting period) for separating paddy fields from drylands and the Wetland index (flooding frequency of the harvesting period) for separating paddy fields from wetlands

$$F(t) = \frac{\sum \text{Flooded Pixel}(t)}{\sum \text{Total} - \sum \text{Bad}}. \tag{3}$$

$F(t)$ denotes the frequency of flooding of a pixel in time period t, $\sum$ Flooded Pixel (t) denotes the total number of times the pixel was observed to be flooded in time period t, $\sum$ Total denotes the number of times the pixel was observed, and $\sum$ Bad denotes the number of times the pixel was unavailable (mainly obscured by clouds).

The paddy index and wetland index were defined as F(Transplanting) and F(Harvesting), respectively. During the transplanting period, cropland that is not planted with rice is typically not flooded. Therefore, the frequency of flooding during this period can be used as a criterion to differentiate between paddy fields and drylands. Conversely, rice is gathered and the cropland does not require flooding during the harvesting period. As a result, the frequency of flooding during this period

is significantly lower. Aquatic vegetation gradually deteriorates, and mudflats continue to experience frequent flooding, resulting in a higher frequency of flooding. By considering the asynchronous flooding patterns between the transplanting and harvesting periods, it is feasible to distinguish between paddy fields and wetlands.

5) Simple Noniterative Clustering and Paddy Field Map Generation: The SNIC algorithm is improved by simple linear iterative clustering algorithm [57], which is a superpixel image segmentation method that can be used for segmenting homogeneous objects. The SNIC algorithm can effectively reduce the "pretzel effect" in pixel classification and is widely used in large-scale land cover classification [58], [59]. The SNIC algorithm has the properties of high computational efficiency, ease of implementation, controllable number of superpixels and compactness for large-scale image segmentation tasks.

This study stacked the paddy index, wetland index, and cropland index, and then segmented them using SNIC. Statistical analysis thresholds of 100 samples each for paddy fields, drylands, wetlands, and forests were used to generate a final map of paddy fields in the Northern Region of China. Thresholds were initially determined by analyzing the distribution of the land samples on the three indices and calculating the percentiles for the paddy field samples. The thresholds were then adjusted according to the purpose of the designed indexes to make the thresholds more acceptable (detailed steps are described in section of the Appendix).

D. Evaluation Analysis

Multiple validation and comparison methods were used to assess the accuracy of the asynchronous flooding and object-based (AF-OB) paddy field maps. Confusion matrices were derived from independent validation samples, and four metrics were calculated to gauge the precision of the paddy field maps: user's accuracy (UA), producer's accuracy (PA), as well as overall accuracy (OA), complemented by the Matthews correlation coefficient (MCC). These metrics, UA, PA, and OA, each range between 0 and 1, with values approaching 1 denoting enhanced performance. The MCC is a correlation coefficient that measures the relationship between observed and predicted binary classifications. It provides more information compared to the Kappa coefficient, especially on unbalanced datasets, and is considered highly reliable [60]. MCC returns a value between –1 and +1. A coefficient of +1 indicates perfect prediction, 0 indicates no better than random prediction, and –1 indicates complete disagreement between prediction and observation. Indicators are calculated as follows:

$$\mathrm{PA} = \frac{\mathrm{TP}}{\mathrm{TP} + \mathrm{FN}} \tag{4}$$

$$\mathrm{UA} = \frac{\mathrm{TP}}{\mathrm{TP} + \mathrm{FP}} \tag{5}$$

$$\mathrm{OA} = \frac{\mathrm{TP} + \mathrm{TN}}{\mathrm{TP} + \mathrm{FP} + \mathrm{TN} + \mathrm{FN}} \tag{6}$$

$$\mathrm{MCC} = \frac{(\mathrm{TP}\times\mathrm{TN}) - (\mathrm{FP}\times\mathrm{FN})}{\sqrt{(\mathrm{TP}+\mathrm{FP})\times(\mathrm{TP}+\mathrm{FN})\times(\mathrm{TN}+\mathrm{FP})\times(\mathrm{TN}+\mathrm{FN})}}. \tag{7}$$

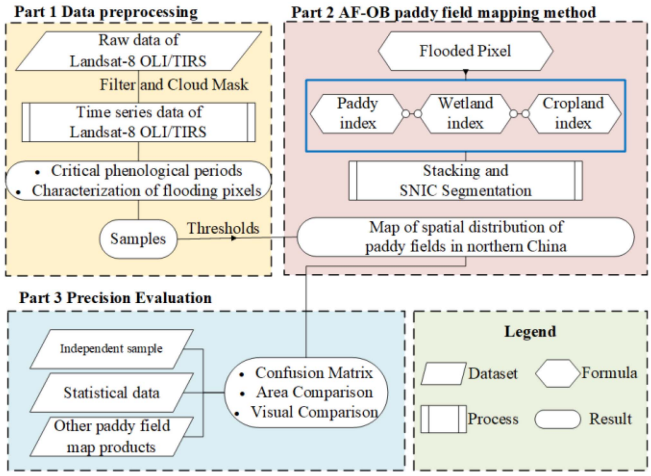

Fig. 4. Flowchart of AF-OB paddy field mapping methods. The AF-OB paddy field mapping method includes three processes: data preprocessing, paddy field map generation and accuracy validation, and a legend showing the meaning of the different boxes.

Here, TP represents true positives, FP stands for false positives, TN corresponds to true negatives, and FN signifies false negatives.

In addition, the China Statistical Yearbook and the third NLRS data were used to validate the area of paddy field maps at the municipal level. Two statistics are used to avoid discrepancies due to statistical methods or human factors [61]. Other paddy field maps were used for visualization in contrast to the AF-OB paddy field maps. Visual comparisons can offer a more intuitive depiction of how data or methodological variances can influence mapping outcomes.

In this study, we first developed paddy index, wetland index, and cropland index based on paddy field phenology information. By utilizing SNIC segmentation and frequency histogram techniques, we generated accurate paddy field maps for the Northern Region of China. The accuracy of our AF-OB paddy map was assessed through the use of confusion matrix, statistical data, and comparison with other existing paddy maps. In addition, we analyzed the distribution characteristics of paddy fields in the Northern Region of China (see Fig. 4).

III. Results

A. Paddy Field Map Generation and Threshold Determination

Fig. 5 shows the role of the designed paddy index, wetland index, and cropland index on image segmentation as well as the results of paddy field mapping. By stacking and segmenting the three indices derived from phenological knowledge, the resulting map showed paddy field patches highlighted in red. Similarly, glaciers, densely forested areas, and wetlands appeared predominantly in green, while perennial water bodies were depicted in yellow. Other land types were represented in blue [see Fig. 5(a)]. These color-coded regions demonstrate the efficacy of AF-OB's paddy field mapping technique in highlighting paddy field information. The boundaries of paddy plots are clear, indicating that these three indices combined with SNIC

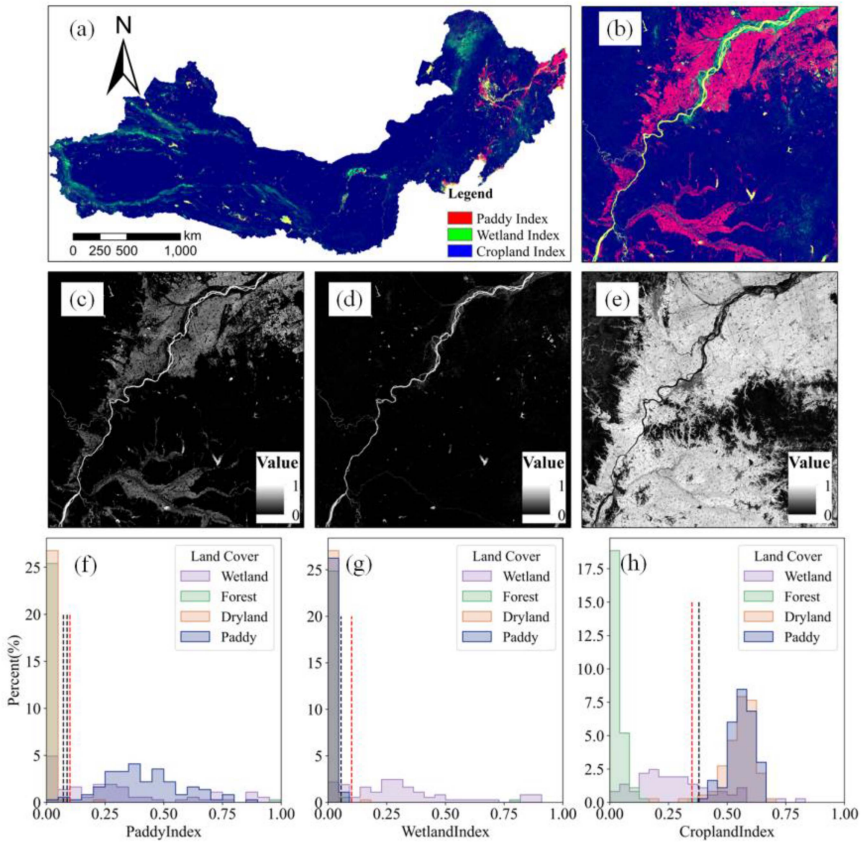

Fig. 5. SNIC segmentation results and detail maps of paddy index, wetland index, and cropland index. (a) SNIC segmentation results were synthesized using the paddy index, wetland index, and cropland index as RGB bands, respectively. (b) Detailed map of SNIC segmentation results. (c)–(e) Paddy index, wetland index, and cropland index before SNIC segmentation. (f)–(h) Histogram of the frequency distribution of each land cover type in the three indices, The black dashed line is the initial threshold obtained by percentile and the red dashed line indicates the adjusted threshold.

can highlight paddy information very well while maintaining spatial integrity and reducing "pretzel noise" [see Fig. 5(b)].

When considering the paddy index alone, it becomes apparent that the frequency of flooding varies apparently from one pixel to another within each paddy field. This variability leads to a lack of precision in the paddy index. The presence of wetlands (including water bodies, floating plants, and mudflats) influences the results [see Fig. 5(c)]. On the other hand, the wetland index effectively highlights the characteristics of wetland areas [see Fig. 5(d)]. The cropland index exhibits a finer texture compared to the other two indices. This characteristic is beneficial in two ways. First, it effectively highlights the information related to cultivated land through its high value. This allows for better identification and distinction of cropland areas in the image analysis. Second, the delicate texture of the cropland index plays a crucial role in preserving the integrity of the patches during the process of image segmentation [see Fig. 5(e)]. By maintaining the fine texture, the boundaries and details of the cropland patches can be preserved, resulting in more precise mapping and analysis.

The frequency distributions of paddy index, wetland index, and cropland index were generated from 100 samples each of paddy, dryland, forest, and wetland in the Northern Region of China. The study used adjusted thresholds of 0.1 for paddy index, 0.1 for wetland index, and 0.35 for cropland index. When the paddy index > 0.1, almost all dry land and forest land are excluded, while paddy fields are retained [see Fig. 5(f)]. When the wetland index < 0.1, most of the wetlands can be excluded [see Fig. 5(g)]. Similarly, when the cropland index > 0.35, cropland is separated from almost all forested land and most wetlands are excluded [see Fig. 5(h)]. The three indices designed for this study allowed us to exclude patches of other land classes while retaining patches of paddy fields as much as possible.

B. Validation Using Confusion Matrix

The results of the confusion matrix calculation show that the OA of the paddy field map obtained by the AF-OB method reaches 94.28%, and the PA and UA are around 90%, while the MCC is 0.88. These acquire indicate that the paddy field map has a high degree of consistency with the actual paddy field distribution (see Table I). From the confusion matrix of subregions, the PA and UA in the more humid Northeast China are both greater than 95%, and the overall accuracy is even 98.25%, which is very high in consistency with the real samples. However, the precision in arid and semi-arid North China is relatively low, with an overall precision of only 88.82%. Such low accuracy is due to the fact that crop cultivation in arid and semi-arid regions is limited by water resources, which leads

TABLE I
CONFUSION MATRIX FOR AF-OB PADDY FIELD MAPPING RESULTS

Confusion Matrix		Ground truth samples		UA (%)	PA (%)	OA (%)	MCC
		non-paddy	paddy				
Total	non-paddy	856	62	93.25	97.38	94.28	0.88
	paddy	23	545	95.95	89.79		
Northeast China	non-paddy	376	13	96.66	99.47	98.25	0.96
	paddy	2	467	99.57	97.29		
Northwest and North China	non-paddy	478	49	90.70	95.79	88.82	0.63
	paddy	21	78	78.79	61.42		

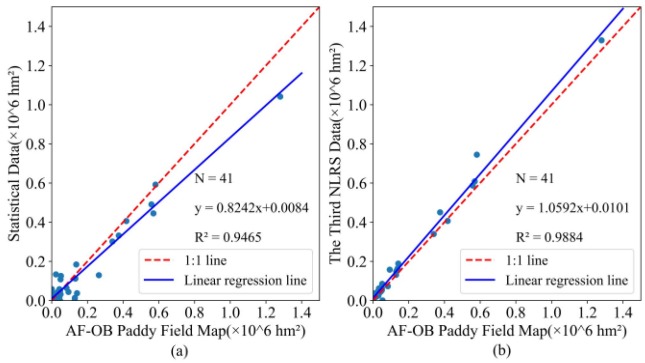

Fig. 6. Comparison of AF-OB paddy field map with the municipal paddy field area in the statistics. (a) Comparison of the results of AF-OB mapping of paddy fields with statistics from the Chinese Statistical Yearbook. (b) Comparison of the results of AF-OB mapping of paddy fields with statistics from the Third NLRS data of China.

to the instability of rice cultivation in this region [62], [63]. The results obtained by the AF-OB method in this study were aggregated from five years of Landsat-8 data, which affected the accuracy of the paddy mapping results. This is why we discuss in Section IV-B the portability of the AF-OB method on Sentinel-2 data in order to address this issue through higher spatiotemporal resolution.

From the results of the confusion matrix, it is seen that the map of paddy fields obtained by the AF-OB method is more inclined to omit some paddy fields and less likely to misclassify nonpaddy fields as paddy fields. It is possible that some paddy fields lacked sufficient valid observations during the transplanting period or were influenced by heavy rainfall during the harvesting period [32]. A threshold was implemented to exclude directly those paddy fields affected by such extreme conditions. We discovered that the AF-OB method exhibited instances of classifying certain wetlands as paddy fields, a common phenomenon observed in many paddy field mapping investigations [9]. However, the AF-OB method markedly mitigates this error, thus enhancing its performance. Considering the design of the paddy index, the wetland index, and the cropland index show an approximately normal or skewed distribution, respectively (see Fig. 6). A threshold can be used to control the source of error, giving these three indices the potential for automatic generation of paddy samples [64]. With automatically generated samples, the use of machine learning that incorporates more features is expected to reduce the errors mentioned above [39].

C. Validation Using Statistical Data

The comparison between the AF-OB paddy map and statistical data from the National Bureau of Statistics of China, as well as data from the Third NLRS data, was conducted across 41 cities in the Northern Region of China.

When comparing the AF-OB paddy map with the statistical data, it was found that the map slightly overestimated the extent of paddy fields. The relationship between the two datasets can be represented by a linear regression equation with a slope of 0.82 and an R^2 value of 0.95 [see Fig. 6(a)]. Such discrepancy could be attributed to the differences in the data generation processes between the statistical data and the AF-OB paddy map. The statistical data rely on local management reporting, which may involve human interference and potential reporting errors. The agreement between the AF-OB paddy map and the Third NLRS data was high with a slope of 1.06 and an R^2 value of 0.99 [see Fig. 6(b)]. This suggests that the spatial data used in both the AF-OB paddy map and the Third NLRS data provide relatively objective and consistent results.

D. Comparison With Other Maps

Three sites were selected to compare the performance of different rice maps. Site 1 was located at the junction of paddy fields and dry land with flat terrain [see Fig. 7(a)–(c)]. Site 2 is located in an area with a more complex topography and striped paddy fields [see Fig. 7(d) and (f)]. Site 3 is distributed with large wetlands and was used to compare the performance of the rice maps in areas where rice and wetlands coexist [see Fig. 7(g) and (i)].

From the comparison between Site 1 and Site 2, the roads between the fields are obvious as NESEA-Rice 10 portrays more details in the flat terrain and densely distributed areas of

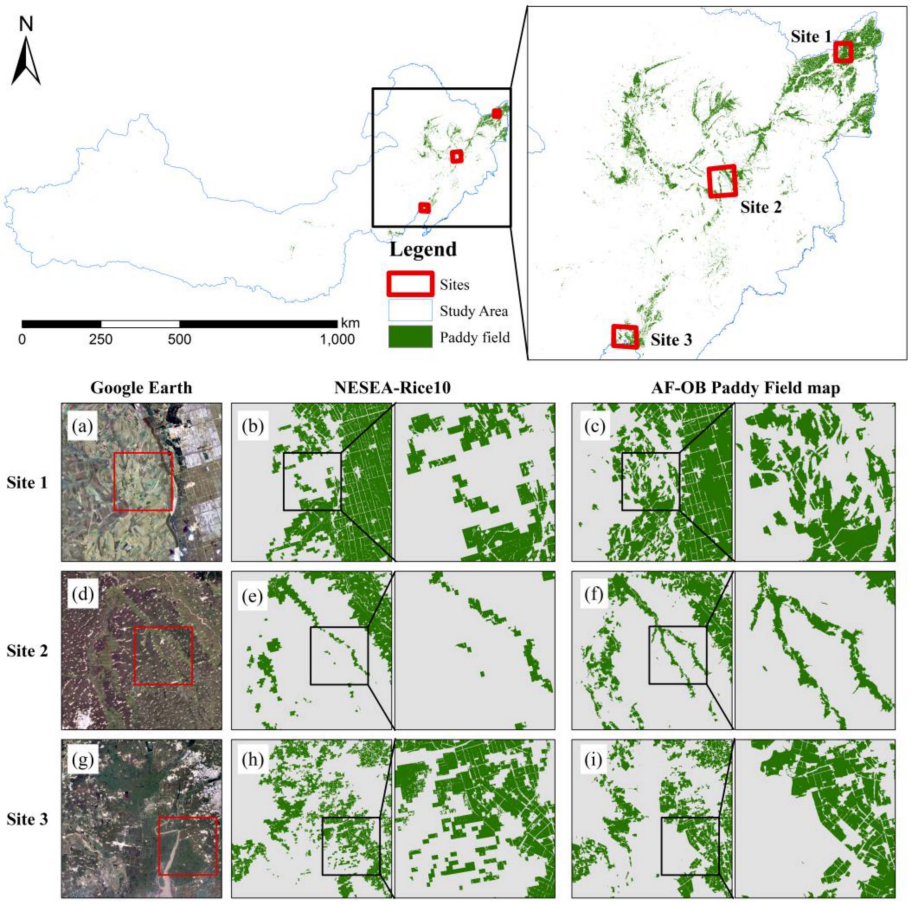

Fig. 7. AF-OB paddy map compared with NESEA-Rice 10 on three sites. (a)–(c) Comparison of paddy field maps in the plains area. (d)–(f) Comparison of paddy field maps in hilly areas. (g)–(i) Comparison of paddy field maps in areas where paddy fields coexist with wetlands.

paddy fields [see Fig. 7(b) and (e)]. This is due to the higher spatial resolution of the Sentinel-2 data used in NESEA-Rice 10. The production of NESEA-Rice 10 uses more other land cover products for masking, resulting in lower accuracy in areas with complex topography or where paddy fields are interspersed with drylands [see Fig. 7(b) and (c)]. In contrast, the AF-OB paddy field map does not use other land cover products as masks and accurately obtains the spatial distribution of paddy fields while retaining most of the details [see Fig. 7(c)–(f)]. The visual performance of the AF-OB paddy map is higher than that of NESEA-Rice 10 in the coexistence area of paddy and wetland, again due to the use of mask data in NESEA-Rice 10 [see Fig. 7(h)–(i)]. Collectively, NESEA-Rice 10 generated a larger area of paddy field maps, but AF-OB paddy field maps were more effective in the Northern Region of China.

E. Temporal Expansion of AF-OB Paddy Filed Map

The area of paddy fields in the Northern Region of China accounts for only 1.54% of the total area, but paddy fields are distributed throughout the study area and show the distribution characteristics of more in the east and less in the west [see Fig. 8(a)–(d)], which is directly related to the climate and topography of the region.

Climatically, wet areas with average annual precipitation greater than 600 mm are distributed with 92.04% paddy fields [see Fig. 8(e)]. In terms of topography, 97% of the paddy fields are located in plains with an elevation of less than 500 m above elevation [see Fig. 8(f)], while the paddy fields tend to be located on the banks of rivers or alluvial plains. Precipitation and runoff bring a lot of organic matter to the paddy fields, providing soil conditions for the paddy fields. The river's abundant water resources provide irrigation conditions for the paddy fields. This is the main reason affecting the spatial distribution of paddy fields in the Northern Region of China. The distribution of rice along rivers is susceptible to river pollution [65], [66], which further exacerbates water stress in arid and semi-arid regions [67]. Our paddy field map also holds the potential to contribute to addressing this issue.

IV. Discussion

A. Improvement of Phenology Algorithm by AF-OB Method

Our model considers not only the relative relationship between bands, but also the fact that increased soil moisture reduces the band reflectance, and limits the average value of the visible band [68], [69]. Unlike most studies that directly use cropland pixels from land use products or use vegetation indices for cropland masks [5], [7], the Cropland index based

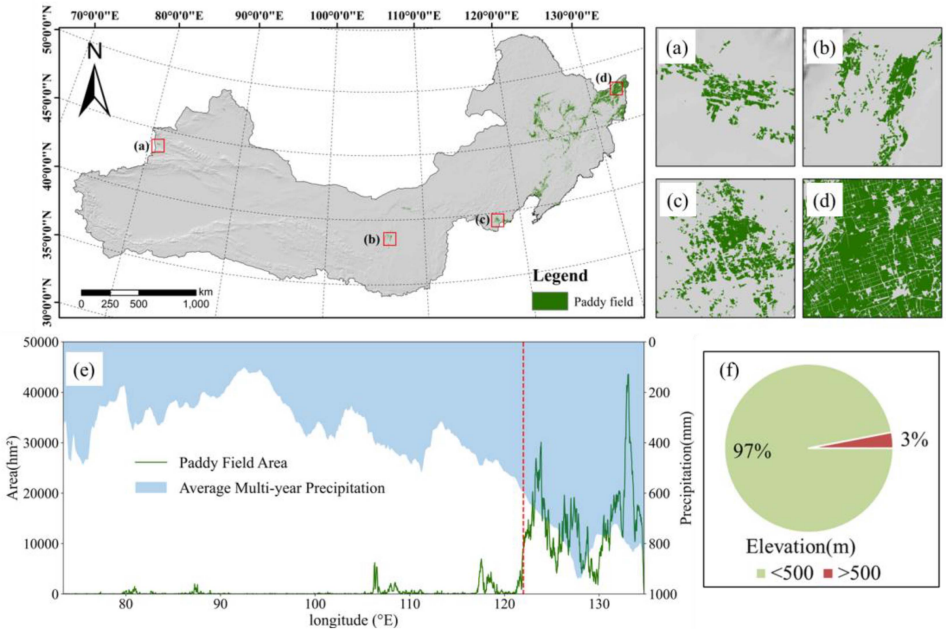

Fig. 8. Map of the spatial distribution of paddy fields in the Northern Region of China. (a)-(d) Detailed map of the spatial distribution of paddy fields; (e) Plot of paddy field area as a function of longitude and precipitation; (f) Distribution of paddy fields about elevation.

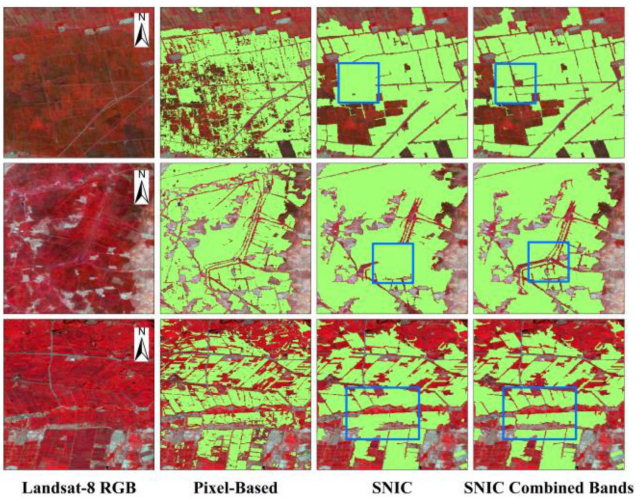

Fig. 9. Effectiveness of mapping paddy fields based on the object method and at combined bands.

on NDVI dynamics was designed to separate croplands in this study. The three indices designed according to the phenological characteristics of the paddy fields in the study area allow us to map the paddy fields more intuitively and to understand the uncertainties in the process of paddy field mapping. The AF-OB method's improved accuracy from 0.12% to 8.25% over the same type of phenology-based rules method and allowed for a larger study area to map the paddy fields, approaching the overall accuracy of the machine learning method in some areas (see Table II). Despite the satisfactory accuracy of the AF-OB method in the north region of China, it is still difficult for the rule-based methods of phenology to achieve a very high accuracy

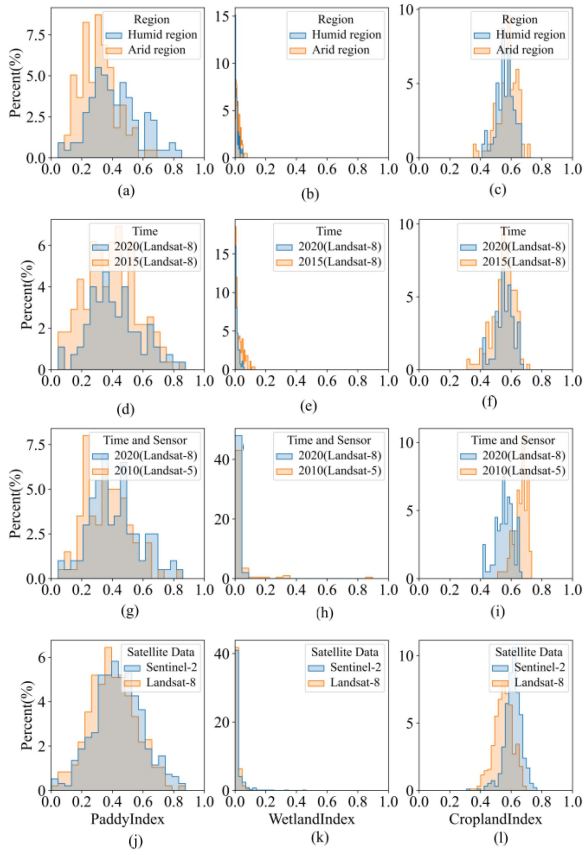

Fig. 10. Stability and applicability tests of the AF-OB paddy field mapping method. (a)–(c) Testing of the AF-OB method in arid and humid regions. (d)–(f) Testing of the AF-OB method at different times; (g)–(i) Testing the use of Landsat-5 for historical paddy field mapping. (j)–(l) Testing of the AF-OB method for spatiotemporal resolution sensors.

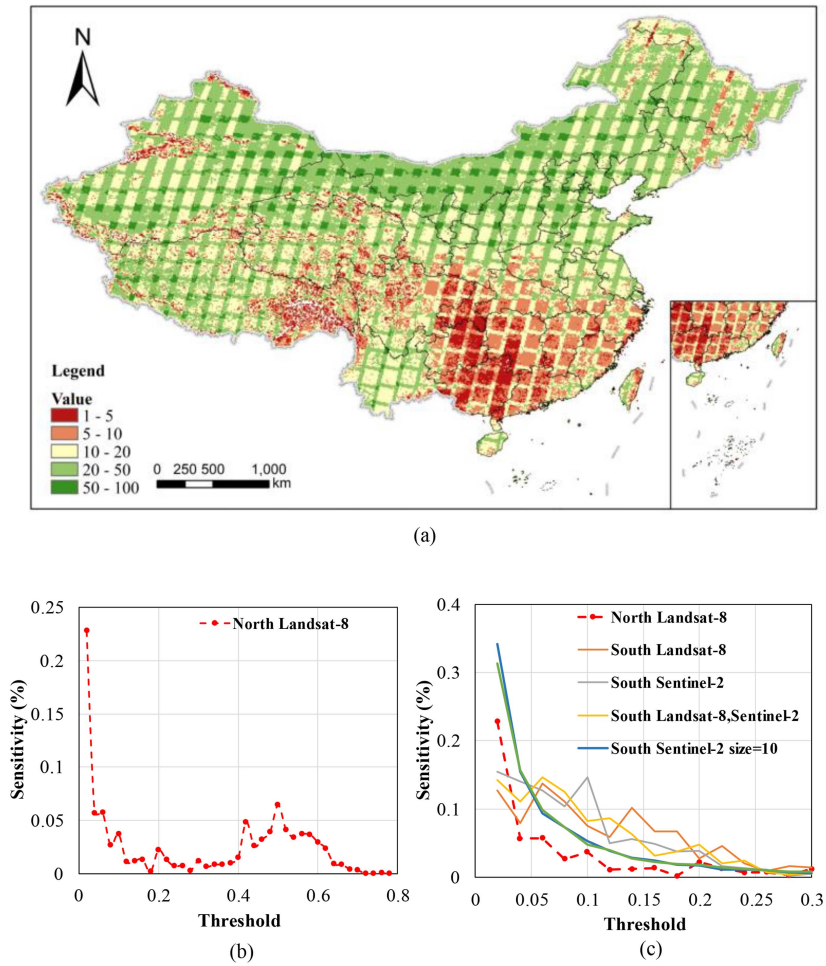

Fig. 11. Sources of uncertainty in the AF-OB method. (a) Number of valid observations during the rice transplanting period in five years of Landsat-8 data. (b) Sensitivity of paddy area to paddy index thresholds in the northern region of China. (c) Sensitivity of paddy area to paddy index thresholds in the southern region of China under different combinations of data and partitioning parameters.

TABLE II
COMPARISON OF THIS STUDY WITH PREVIOUS LITERATURE

Id	Sensor used	Resolution	Study Area	Method	OA (%)	References
1	Sentinel-2 MSI	10 m	Northeast China	SVM	98.64–98.89	Ni et al. [1]
2	Sentinel-1 SAR	10 m	Five sites in China and the United States	SAR changes in "water-vegetation" characteristics	88.00–95.00	Xu et al. [2]
3	Landsat-7 ETM+; Landsat-8 OLI/TIRS	30 m	The Sanjiang Plain, China	Non-cropland mask; Flooding signal detection	88.67–97.32	Qin et al. [5]
4	Landsat-7 ETM+; Landsat-8 OLI/TIRS	30 m	China	Non-cropland mask; Flooding signal detection	83.00–90.00	Wei et al. [7]
5	Landsat-5 TM; Landsat-7 ETM+	30 m	Japan	Non-cropland mask; Flooding signal detection	83.30–95.00	Carrasco et al. [9]
6	Landsat-8 OLI/TIRS	30 m	The Northern Region of China	Flooding signal detection; Characteristics design based on phenology	88.82–98.25	This study

over the whole large region using a uniform threshold [9]. The overall accuracy of the AF-OB method varies by almost 10% between the northeast and northwest of China, which is in line with the shortcomings of the same type algorithms (see Table II).

Segmentation algorithms such as SNIC and other superpixels are very important in paddy field mapping work [70], especially for unsupervised classification of phenology algorithms. Homogeneous objects can be very discrete in some of the features due to mixed pixels or outliers. This can exacerbate the "pretzel effect" caused by pixel-based classification [71], whereas superpixel segmentation algorithms can consider multiple bands or features at the same time to minimize the impact of partially discrete features [72]. Supplementary experiment 2 shows that the mapping results based on paddy field objects segmented by the SNIC algorithm effectively eliminates the "pretzel effect" compared to the pixel-based results. The object based approach also loses some details such as field roads during image segmentation, whereas combining more bands and features during image segmentation can recover some of the details (see Fig. 9).

Overall, the AF-OB method does not introduce existing land use products, but rather the three indices designed with image segmentation to get better results for mapping paddy fields.

B. Stability of the AF-OB Method Across Spatiotemporal and Sensors

The study employed the designed paddy index, wetland index, and cropland index to assess the stability of thresholds in the AF-OB method across different temporal and sensor variations. The frequency distributions of the three indices in the AF-OB method exhibited similar patterns in both arid and humid regions [see Fig. 10(a)–(c)]. However, specifically for the paddy index, the frequency distribution was found to be flatter in humid regions compared to arid regions. This observation suggests that there is a tendency for rice replanting to occur during a more concentrated period in arid regions, while the period of rice replanting tends to be more spread out or decentralized in humid regions. Under the condition that Landsat-8 is used in both 2015 and 2020, there is essentially no difference in the distribution of the paddy field samples on the three indices [see Fig. 10(d)–(f)]. This is due to the fact that the change in time does not change the flooding dynamics and NDVI dynamics of the paddy fields. The potential of the AF-OB paddy mapping method for past paddy mapping using Landsat-5 TM was evaluated in the same way. It was shown that the change of sensor and time did not change the frequency distribution of paddy field objects on the paddy index and wetland index [see Fig. 10(g) and (h)]. However, the Cropland index was shifted [see Fig. 10(i)], probably due to differences in NDVI calculated by different sensors [73], [74].

The potential of Sentinel-2 for paddy mapping using the AF-OB method was validated as Sentinel-2 has the potential for annual rice mapping due to its shorter revisit period [33]. Except for a mild shift in the Cropland index due to sensor differences, Sentinel-2's frequency distributions at the three indices are essentially the same [see Fig. 10(j)–(l)]. This demonstrates that the AF-OB method is applicable to Sentinel-2 despite the fact that Sentinel-2 differs from Landsat-8 in terms of revisit period and spatial resolution.

The test results confirm the stability of the AF-OB method across various spatial, temporal, and sensor conditions. It is important to note that while the threshold value of the AF-OB method remains relatively stable, adjustments may be necessary when changing sensors due to potential offset issues in the cropland index. By appropriately calibrating and adapting the threshold value, accurate results for paddy field mapping can be achieved.

C. Limitations of the AF-OB Method

Unsupervised classification algorithms based on phenology are effective in paddy mapping depending on how the key phenological periods are defined. The three periods defined by the AF-OB method are limited to single-season rice in the Northern Region of China because they are designed for single-season rice. Therefore, it is challenging to attain the desired results in regions of the south where double-cropped rice is extensively grown. The concept of the AF-OB method deserves recognition due to the variations in "soil-water-vegetation" observed in both double-season rice and single-season rice [6]. It remains feasible to apply similar principles in identifying paddy fields by establishing the relevant phenological period.

Supplementary experiments 1 showed that the sources of uncertainty of the AF-OB method when used in southern China are mainly the reduction of effective satellite observations due to cloud shading [see Fig. 11(a)]. Parameter tuning of the image segmentation algorithm due to differences in paddy patch size also leads to uncertainty [see Fig. 11(b) and (c)].

The accuracy of the AF-OB rice mapping method depends largely on the monitoring of flood signals during rice planting. Flood signals in rice fields can be effectively captured by combining data from multiple sources for a wider range of spatial and temporal observations [23], [75], [76]. This also helps to extend the AF-OB method or its idea to areas with humid, cloudy, and rainy climates. The parameters of the image segmentation algorithm also need to be adjusted in this process by taking into account the differences in shape and size of paddy field patches between different regions [see Fig. 11(c)].

V. Conclusion

This study proposes a robust asynchronous flood and object-based remote sensing mapping framework for paddy fields using dense Landsat-8 satellite imagery within Google Earth Engine, eliminating the need for external land cover product masks. By delineating critical periods for paddy field mapping and using three specific indices grounded in inundation patterns and NDVI dynamics during these periods, our model offers an innovative strategy. Superpixel segmentation technique was introduced and effectively mitigated the "pretzel effect." The efficacy of our model is evaluated within Northern Region of China, a vast and climatically diverse area. Our results show that the distribution of paddy fields in the northern region of China is highly correlated with the topography and water system, which

is consistent with the real situation. The proposed paddy mapping model substantially enhances accuracy by 0.12% to 8.25% compared to the two conventional models. The resulting paddy field mappings consistently exhibit high R^2 values, ranging from 0.95 to 0.99, when contrasted with statistical data. Furthermore, our model demonstrates consistent thresholds across time, space, and sensors, ensuring method portability.

The AF-OB method has limitations for applications in areas with cloudy climates or small patches of paddy fields. Despite this, the AF-OB method exhibits potential for expansion into national mapping of paddy fields by incorporating joint multisource data.

REFERENCES

[1] R. Ni et al., "An enhanced pixel-based phenological feature for accurate paddy rice mapping with Sentinel-2 imagery in Google Earth Engine," *ISPRS J. Photogrammetry Remote Sens.*, vol. 178, pp. 282–296, Aug. 2021.

[2] S. Xu et al., "A robust index to extract paddy fields in cloudy regions from SAR time series," *Remote Sens. Environ.*, vol. 285, 2023, Art. no. 113374.

[3] Joint FAO, OIE, WHO, and WTO Statement on Influenza A (H1N1) and the Safety of Pork, FAO, Rome, Italy, 2009.

[4] H. Wu et al., "AsiaRiceYield4km: Seasonal rice yield in Asia from 1995 to 2015," *Earth System Sci. Data*, vol. 15, no. 2, pp. 791–808, 2023.

[5] Y. Qin et al., "Mapping paddy rice planting area in cold temperate climate region through analysis of time series Landsat 8 (OLI), Landsat 7 (ETM+) and MODIS imagery," *ISPRS J. Photogrammetry Remote Sens.*, vol. 105, pp. 220–233, 2015.

[6] J. Dong and X. Xiao, "Evolution of regional to global paddy rice mapping methods: A review," *ISPRS J. Photogrammetry Remote Sens.*, vol. 119, pp. 214–227, 2016.

[7] J. Wei, Y. Cui, W. Luo, and Y. Luo, "Mapping paddy rice distribution and cropping intensity in China from 2014 to 2019 with Landsat images, effective flood signals, and Google Earth Engine," *Remote Sens.*, vol. 14, no. 3, 2022, Art. no. 759.

[8] Y. Wang, L. Zhou, Q. Jia, and W. Yu, "Water use efficiency of a rice paddy field in Liaohe Delta, Northeast China," *Agricultural Water Manage.*, vol. 187, pp. 222–231, 2017.

[9] L. Carrasco, G. Fujita, K. Kito, and T. Miyashita, "Historical mapping of rice fields in Japan using phenology and temporally aggregated landsat images in Google Earth Engine," *ISPRS J. Photogrammetry Remote Sens.*, vol. 191, pp. 277–289, 2022.

[10] K. Liu, X. Li, S. Wang, and X. Zhang, "Unrevealing past and future vegetation restoration on the Loess Plateau and its impact on terrestrial water storage," *J. Hydrol.*, vol. 617, 2023, Art. no. 129021.

[11] K. Liu, H. Su, X. Li, and S. Chen, "Development of a 250-m downscaled land surface temperature data set and its application to improving remotely sensed evapotranspiration over large landscapes in northern China," *IEEE Trans. Geosci. Remote Sens.*, vol. 60, 2020, Art. no. 5000112.

[12] X. Cai and C. Ringler, "Balancing agricultural and environmental water needs in China: Alternative scenarios and policy options," *Water Policy*, vol. 9, no. S1, pp. 95–108, 2007.

[13] V. Niva, J. Cai, M. Taka, M. Kummu, and O. Varis, "China's sustainable water-energy-food nexus by 2030: Impacts of urbanization on sectoral water demand," *J. Cleaner Prod.*, vol. 251, 2020, Art. no. 119755.

[14] X. Cai, "Water stress, water transfer and social equity in Northern China—Implications for policy reforms," *J. Environ. Manage.*, vol. 87, no. 1, pp. 14–25, 2008.

[15] J. Li, Z. Liu, C. He, H. Yue, and S. Gou, "Water shortages raised a legitimate concern over the sustainable development of the drylands of northern China: Evidence from the water stress index," *Sci. Total Environ.*, vol. 590, pp. 739–750, 2017.

[16] J. Wei, Y. Cui, S. Zhou, and Y. Luo, "Regional water-saving potential calculation method for paddy rice based on remote sensing," *Agricultural Water Manage.*, vol. 267, 2022, Art. no. 107610.

[17] J. M. Yeom, S. Jeong, R. C. Deo, and J. Ko, "Mapping rice area and yield in northeastern Asia by incorporating a crop model with dense vegetation index profiles from a geostationary satellite," *GIScience Remote Sens.*, vol. 58, no. 1, pp. 1–27, 2021.

[18] D. M. G. de la Torre, J. Gao, and C. Macinnis-Ng, "Remote sensing-based estimation of rice yields using various models: A critical review," *Geo-Spatial Inf. Sci.*, vol. 24, no. 4, pp. 580–603, 2021.

[19] M. Weiss, F. Jacob, and G. Duveiller, "Remote sensing for agricultural applications: A meta-review," *Remote Sens. Environ.*, vol. 236, 2020, Art. no. 111402.

[20] K. Liu, X. Li, S. Wang, and X. Gao, "Assessing the effects of urban green landscape on urban thermal environment dynamic in a semiarid city by integrated use of airborne data, satellite imagery and land surface model," *Int. J. Appl. Earth Observation Geoinf.*, vol. 107, 2022, Art. no. 102674.

[21] C. Ma et al., "Temperature and emissivity retrieval from hyperspectral thermal infrared data using dictionary-based sparse representation for emissivity," *IEEE Trans. Geosci. Remote Sens.*, vol. 61, 2023, Art. no. 5002016.

[22] S. Chauhan, R. Darvishzadeh, M. Boschetti, M. Pepe, and A. Nelson, "Remote sensing-based crop lodging assessment: Current status and perspectives," *ISPRS J. Photogrammetry Remote Sens.*, vol. 151, pp. 124–140, 2019.

[23] Y. Cai, H. Lin, and M. Zhang, "Mapping paddy rice by the object-based random forest method using time series Sentinel-1/Sentinel-2 data," *Adv. Space Res.*, vol. 64, no. 11, pp. 2233–2244, 2019.

[24] M. Waleed et al., "Evaluating the efficiency of coarser to finer resolution multispectral satellites in mapping paddy rice fields using GEE implementation," *Sci. Rep.*, vol. 12, no. 1, 2022, Art. no. 13210.

[25] L. R. Mansaray, F. Wang, J. Huang, L. Yang, and A. S. Kanu, "Accuracies of support vector machine and random forest in rice mapping with Sentinel-1A, Landsat-8 and Sentinel-2A datasets," *Geocarto Int.*, vol. 35, no. 10, pp. 1088–1108, 2020.

[26] X. Li, L. Li, L. Chen, T. Zhang, J. Xiao, and L. Chen, "Random forest estimation and trend analysis of PM2. 5 concentration over the Huaihai Economic Zone, China (2000–2020)," *Sustainability*, vol. 14, no. 14, 2022, Art. no. 8520.

[27] H. Bazzi et al., "Mapping paddy rice using Sentinel-1 SAR time series in Camargue, France," *Remote Sens.*, vol. 11, no. 7, 2019, Art. no. 887.

[28] X.-Z. Pan, S. Uchida, Y. Liang, A. Hirano, and B. Sun, "Discriminating different landuse types by using multitemporal NDXI in a rice planting area," *Int. J. Remote Sens.*, vol. 31, no. 3, pp. 585–596, 2010.

[29] A. E. Maxwell, T. A. Warner, and F. Fang, "Implementation of machine-learning classification in remote sensing: An applied review," *Int. J. Remote Sens.*, vol. 39, no. 9, pp. 2784–2817, 2018.

[30] M. Sheykhmousa, M. Mahdianpari, H. Ghanbari, F. Mohammadimanesh, P. Ghamisi, and S. Homayouni, "Support vector machine versus random forest for remote sensing image classification: A meta-analysis and systematic review," *IEEE J. Sel. Topics Appl. Earth Observ. Remote Sens.*, vol. 13, pp. 6308–6325, 2020.

[31] C. Small, "Grand challenges in remote sensing image analysis and classification," *Front. Remote Sens.*, vol. 1, 2021, Art. no. 605220.

[32] R. Zhao, Y. Li, and M. Ma, "Mapping paddy rice with satellite remote sensing: A review," *Sustainability*, vol. 13, no. 2, 2021, Art. no. 503.

[33] J. Han et al., "NESEA-Rice10: High-resolution annual paddy rice maps for Northeast and Southeast Asia from 2017 to 2019," *Earth System Sci. Data*, vol. 13, no. 12, pp. 5969–5986, 2021.

[34] P. Zhan, W. Zhu, and N. Li, "An automated rice mapping method based on flooding signals in synthetic aperture radar time series," *Remote Sens. Environ.*, vol. 252, 2021, Art. no. 112112.

[35] W. Liu, J. Dong, K. Xiang, S. Wang, W. Han, and W. Yuan, "A sub-pixel method for estimating planting fraction of paddy rice in Northeast China," *Remote Sens. Environ.*, vol. 205, pp. 305–314, 2018.

[36] B. Qiu, W. Li, Z. Tang, C. Chen, and W. Qi, "Mapping paddy rice areas based on vegetation phenology and surface moisture conditions," *Ecological Indicators*, vol. 56, pp. 79–86, 2015.

[37] X. Xiao et al., "Mapping paddy rice agriculture in southern China using multi-temporal MODIS images," *Remote Sens. Environ.*, vol. 95, no. 4, pp. 480–492, 2005.

[38] T. Sakamoto, N. Van Nguyen, A. Kotera, H. Ohno, N. Ishitsuka, and M. Yokozawa, "Detecting temporal changes in the extent of annual flooding within the Cambodia and the Vietnamese Mekong Delta from MODIS time-series imagery," *Remote Sens. Environ.*, vol. 109, no. 3, pp. 295–313, 2007.

[39] C. Zhang, H. Zhang, and S. Tian, "Phenology-assisted supervised paddy rice mapping with the Landsat imagery on Google Earth Engine: Experiments in Heilongjiang Province of China from 1990 to 2020," *Comput. Electron. Agriculture*, vol. 212, 2023, Art. no. 108105.

[40] D. Li et al., "Four decades of hydrological response to vegetation dynamics and anthropogenic factors in the Three-North Region of China and Mongolia," *Sci. Total Environ.*, vol. 857, 2023, Art. no. 159546.
[41] X. Liu, H. Li, S. Wang, K. Liu, L. Li, and D. Li, "Ecological security assessment of 'grain-for-green' program typical areas in Northern China based on multi-source remote sensing data," *Remote Sens.*, vol. 15, no. 24, 2023, Art. no. 5732.
[42] H. Li et al., "Relationship between carbon pool changes and environmental changes in arid and semi-arid steppe—A two decades study in Inner Mongolia, China," *Sci. Total Environ.*, 2023, Art. no. 164930.
[43] H. Du, X. Liu, X. Jia, S. Li, and Y. Fan, "Assessment of the effects of ecological restoration projects on soil wind erosion in northern China in the past two decades," *CATENA*, vol. 215, 2022, Art. no. 106360.
[44] K. Liu, X. Li, S. Wang, and H. Zhang, "A robust gap-filling approach for European Space Agency Climate Change Initiative (ESA CCI) soil moisture integrating satellite observations, model-driven knowledge, and spatiotemporal machine learning," *Hydrol. Earth System Sci.*, vol. 27, no. 2, pp. 577–598, 2023.
[45] K. Liu, X. Li, S. Wang, and G. Zhou, "Past and future adverse response of terrestrial water storages to increased vegetation growth in drylands," *npj Climate Atmospheric Sci.*, vol. 6, no. 1, 2023, Art. no. 113.
[46] D. P. Roy et al., "Landsat-8: Science and product vision for terrestrial global change research," *Remote Sens. Environ.*, vol. 145, pp. 154–172, 2014.
[47] S. Viswambharan, I. T. Kumaramkandath, and J. A. Tali, "A geospatial approach in monitoring the variations on surface soil moisture and vegetation water content: A case study of Palakkad District, Kerala, India," *Environ. Earth Sci.*, vol. 81, no. 20, 2022, Art. no. 494.
[48] X. Zhao, K. Nishina, A. Ito, Y. Masutomi, and S. Li, "Mapping rice and soybean calendars based on different algorithms," in *Proc. AGU Fall Meet. Abstr.*, 2022, vol. 2022, Paper GC31A-08.
[49] X. Zhao, K. Nishina, T. K. Akitsu, L. Jiang, Y. Masutomi, and K. N. Nasahara, "Feature-based algorithm for large-scale rice phenology detection based on satellite images," *Agricultural Forest Meteorol.*, vol. 329, 2023, Art. no. 109283.
[50] J. B. Tao, X. Y. Zhang, Q. F. WU, and W. Yun, "Mapping winter rapeseed in South China using Sentinel-2 data based on a novel separability index," *J. Integrative Agriculture*, vol. 22, no. 6, pp. 1645–1657, 2023.
[51] B. Qiu et al., "Maps of cropping patterns in China during 2015–2021," *Sci. Data*, vol. 9, no. 1, 2022, Art. no. 479.
[52] F. Xuan et al., "Mapping crop type in Northeast China during 2013–2021 using automatic sampling and tile-based image classification," *Int. J. Appl. Earth Observation Geoinf.*, vol. 117, 2023, Art. no. 103178.
[53] H. Li et al., "Development of a 10-m resolution maize and soybean map over China: Matching satellite-based crop classification with sample-based area estimation," *Remote Sens. Environ.*, vol. 294, 2023, Art. no. 113623.
[54] X. Chen et al., "Toward sustainable land use in China: A perspective on China's national land surveys," *Land Use Policy*, vol. 123, 2022, Art. no. 106428.
[55] T. Le Toan et al., "Rice crop mapping and monitoring using ERS-1 data based on experiment and modeling results," *IEEE Trans. Geosci. Remote Sens.*, vol. 35, no. 1, pp. 41–56, Jan. 1997.
[56] C. Zhu, D. Lu, D. Victoria, and L. V. Dutra, "Mapping fractional cropland distribution in Mato Grosso, Brazil using time series MODIS enhanced vegetation index and Landsat thematic mapper data," *Remote Sens.*, vol. 8, no. 1, 2016, Art. no. 22.
[57] R. Achanta, A. Shaji, K. Smith, A. Lucchi, P. Fua, and S. Süsstrunk, "SLIC superpixels compared to state-of-the-art superpixel methods," *IEEE Trans. Pattern Anal. Mach. Intell.*, vol. 34, no. 11, pp. 2274–2282, Nov. 2012.
[58] H. Li et al., "Automatic mapping of national surface water with OpenStreetMap and Sentinel-2 MSI data using deep learning," *Int. J. Appl. Earth Observation Geoinf.*, vol. 104, 2021, Art. no. 102571.
[59] M. Wang et al., "Interannual changes of coastal aquaculture ponds in China at 10-m spatial resolution during 2016–2021," *Remote Sens. Environ.*, vol. 284, 2023, Art. no. 113347.
[60] D. Chicco, M. J. Warrens, and G. Jurman, "The Matthews correlation coefficient (MCC) is more informative than Cohen's Kappa and Brier score in binary classification assessment," *IEEE Access*, vol. 9, pp. 78368–78381, 2021.
[61] G. Liu et al., "On the accuracy of official Chinese crop production data: Evidence from biophysical indexes of net primary production," *Proc. Nat. Acad. Sci.*, vol. 117, no. 41, pp. 25434–25444, 2020.
[62] X. Tong et al., "The forgotten land use class: Mapping of fallow fields across the Sahel using Sentinel-2," *Remote Sens. Environ.*, vol. 239, 2020, Art. no. 111598.
[63] A. M. Abdi, N. Boke-Olén, D. E. Tenenbaum, T. Tagesson, B. Cappelaere, and J. Ardö, "Evaluating water controls on vegetation growth in the semi-arid Sahel using field and Earth observation data," *Remote Sens.*, vol. 9, no. 3, 2017, Art. no. 294.
[64] N. You, J. Dong, J. Li, J. Huang, and Z. Jin, "Rapid early-season maize mapping without crop labels," *Remote Sens. Environ.*, vol. 290, 2023, Art. no. 113496.
[65] K. I. Shinozuka, M. Chiwa, K. Nakamura, S. Nagao, and A. Kume, "Stream water nitrogen eutrophication during non-irrigated periods in a paddy-dominated agricultural basin in a snowfall area in Japan," *Water, Air, Soil Pollut.*, vol. 227, pp. 1–11, 2016.
[66] M. Lamers, M. Anyusheva, N. La, V. V. Nguyen, and T. Streck, "Pesticide pollution in surface-and groundwater by paddy rice cultivation: A case study from Northern Vietnam," *Clean–Soil, Air, Water*, vol. 39, no. 4, pp. 356–361, 2011.
[67] A. Fernández-Cirelli, J. L. Arumí, D. Rivera, and P. W. Boochs, "Environmental effects of irrigation in arid and semi-arid regions," *Chilean J. Agricultural Res.*, vol. 69, pp. 27–40, 2009.
[68] M. F. Baumgardner, L. F. Silva, L. L. Biehl, and E. R. Stoner, "Reflectance properties of soils," *Adv. Agronomy*, vol. 38, pp. 1–44, 1986.
[69] L. Weidong, F. Baret, G. Xingfa, T. Qingxi, Z. Lanfen, and Z. Bing, "Relating soil surface moisture to reflectance," *Remote Sens. Environ.*, vol. 81, nos. 2/3, pp. 238–246, 2002.
[70] P. D. Dao and Y.-A. Liou, "Object-based flood mapping and affected rice field estimation with landsat 8 OLI and MODIS data," *Remote Sens.*, vol. 7, no. 5, pp. 5077–5097, 2015.
[71] X. Li, T. Wu, K. Liu, Y. Li, and L. Zhang, "Evaluation of the Chinese fine spatial resolution hyperspectral satellite TianGong-1 in urban land-cover classification," *Remote Sens.*, vol. 8, no. 5, 2016, Art. no. 438.
[72] Y. Zhao, F. Su, and F. Yan, "Novel semi-supervised hyperspectral image classification based on a superpixel graph and discrete potential method," *Remote Sens.*, vol. 12, no. 9, 2020, Art. no. 1528.
[73] J. Franke, V. Heinzel, and G. Menz, "Assessment of NDVI-differences caused by sensor specific relative spectral response functions," in *Proc. IEEE Int. Symp. Geosci. Remote Sens.*, 2006, pp. 1138–1141.
[74] X. Fan and Y. Liu, "A comparison of NDVI intercalibration methods," *Int. J. Remote Sens.*, vol. 38, no. 19, pp. 5273–5290, 2017.
[75] M. Saadat, S. T. Seydi, M. Hasanlou, and S. Homayouni, "A convolutional neural network method for rice mapping using time-series of Sentinel-1 and Sentinel-2 imagery," *Agriculture*, vol. 12, no. 12, 2022, Art. no. 2083.
[76] Q. Jiang et al., "Mapping paddy rice planting area in Dongting Lake Area combining time series Sentinel-1 and Sentinel-2 images," *Remote Sens.*, vol. 15, no. 11, 2023, Art. no. 2794.

Long Li is currently working toward the Ph.D. degree in cartography and GIS in the Aerospace Information Research Institute, Chinese Academy of Sciences, Beijing, China.

His research interests include remote sensing extraction of agricultural information.

Daoqin Zhou received the B.S. degree in remote sensing applications from Wuhan University, Wuhan, China, in 2006.

She is currently working with the Third Surveying and Mapping Institute of Guizhou Province, Guiyang, China. Her research interests include remote sensing information extraction.

Kai Liu received the M.S. degree in electronic and communication engineering from the Institute of Remote Sensing and Digital Earth, Beijing, China, in 2013, and the Ph.D. degree in cartography and geographical information system from the Institute of Geographic Sciences and Nature Resource Research, Beijing, in 2016.

His research interests include the application of thermal infrared and hydrological remote sensing methods to the study of land use and anthropogenic activities, urban heat island, and surface energy and water balance.

Tian Shi received the B.S. degree in application of new technologies in mapping and geographic information from the Guizhou University of Technology, Guiyang, China, in 2003.

He is currently working with the Third Surveying and Mapping Institute of Guizhou Province, Guiyang. His research interests include remote sensing information extraction.

Chou Xie received the B.Eng. degree in photogrammetry and remote sensing from Wuhan University, Wuhan, China, in 2005, and the Ph.D. degree in cartography and geographic information system from Graduate University of Chinese Academy of Sciences, Beijing, China, in 2008.

He is currently a Professor of remote sensing with the Aerospace Information Research Institute, Chinese Academy of Sciences, Beijing, China. His research interests include remote sensing (mainly InSAR and GNSS) and their applications to geohazards (e.g., earthquakes, landslides, and land subsidence).

Shudong Wang received the Ph.D. degree in cartography and geographic information system from the State Key Laboratory of Remote Sensing, Institute of Remote Sensing and Digital Earth, Normal University, Beijing, China, in 2007.

He is currently an Research Fellow with the Aerospace Information Research Institute, Chinese Academy of Sciences, Beijing. His research interests include optical remote sensing and its application in ecological and environment field.

Hang Li received the Ph.D. degree in mineralogy, petrology and mineral deposit from Jilin University, Changchun, China, in 2022.

In 2022, he entered the postdoctoral research station of Geography in the Institute of Aerospace Information Innovation, Chinese Academy of Sciences, Beijing, China, and has been working ever since. His research interests include the genetic and tectonic background analysis of granitic rocks, remote sensing inversion of carbon pools in terrestrial ecosystems, and remote sensing observation and attribution analysis of changes in terrestrial ecosystems.

Guannan Dong is currently working toward the Ph.D. degree in the Institute of Geographic Sciences and Natural Resources Research, Chinese Academy of Sciences, Beijing, China.

His current research interests include urban remote sensing, urban carbon assessment, and model design.

Xueke Li received the M.S. degree in cartography and geographic information systems from the Institute of Remote Sensing and Digital Earth, Chinese Academy of Sciences, Beijing, China, in 2014, and the Ph.D. degree in geography from the University of Connecticut, Storrs, CT, USA, in 2019.

Since 2023, she has been a Postdoctoral Fellow with the Department of Earth and Environmental Science, University of Pennsylvania, Philadelphia, PA, USA. Her current research interests include extreme weather/climate and the associated drivers, mechanisms, and impacts.